Water fluxes pattern growth and identity in shoot meristems

Juan Alonso-Serra, Ibrahim Cheddadi, Annamaria Kiss, Guillaume Cerutti, Marianne Lang, Sana Dieudonné, Claire Lionnet, Christophe Godin, Olivier Hamant

nature communications

Article

https://doi.org/10.1038/s41467-024-51099-x

Water fluxes pattern growth and identity in shoot meristems

Received: 27 October 2023

Accepted: 28 July 2024

Published online: 13 August 2024

Check for updates

Juan Alonso-Serra[1,3,4] ✉, Ibrahim Cheddadi[1,2,4], Annamaria Kiss[1], Guillaume Cerutti[1], Marianne Lang[1], Sana Dieudonné[1], Claire Lionnet[1], Christophe Godin[1] & Olivier Hamant[1] ✉

In multicellular organisms, tissue outgrowth creates a new water sink, modifying local hydraulic patterns. Although water fluxes are often considered passive by-products of development, their contribution to morphogenesis remains largely unexplored. Here, we mapped cell volumetric growth across the shoot apex in *Arabidopsis thaliana*. We found that, as organs grow, a subpopulation of cells at the organ-meristem boundary shrinks. Growth simulations using a model that integrates hydraulics and mechanics revealed water fluxes and predicted a water deficit for boundary cells. *In planta*, a water-soluble dye preferentially allocated to fast-growing tissues and failed to enter the boundary domain. Cell shrinkage next to fast-growing domains was also robust to different growth conditions and different topographies. Finally, a molecular signature of water deficit at the boundary confirmed our conclusion. Taken together, we propose that the differential sink strength of emerging organs prescribes the hydraulic patterns that define boundary domains at the shoot apex.

During development, multicellular tissues are patterned by biochemical and mechanical cues[1–7]. This is notably the case at the shoot apical meristem (SAM), which contains the plant stem cell niche and where hormone and peptide patterns define the different zones and their function: self-maintenance (central zone (CZ)), organ production and identity (peripheral zone (PZ)) and organ separation and axillary meristem initiation (boundary zone (BZ)). In particular, differential growth together with tissue shape prescribe a stereotypical pattern of mechanical stress, impacting cytoskeleton behavior[8], hormone carrier polarity[9,10], chromatin status[11], and gene expression[12] in a feedback loop. Other physical cues, such as hypoxia[13], have been integrated into this picture more recently. However, until now, the role of water has been considered non-limiting for morphogenesis in aboveground organs, with water playing essentially no role in the patterning per se.

Belowground, fluctuations in water availability modulate the developmental plasticity of roots[14,15]. In this organ, water conditions also affect endogenous water fluxes, thereby redistributing the plant hormone abscisic acid (ABA). ABA signaling then closes symplasmic pathways leading to repression of lateral organ growth under water deficit[16]. Lateral root development is achieved by reversion of the previous mechanism and by further localized modifications of tissue hydraulics[17]. Environmental signals also induce changes to the symplasmic fluxes in the shoots in an ABA-dependent manner[18,19]. However, most above-mentioned examples represent hydraulic fluctuations induced by the environment, while less is known about growth-induced hydraulic patterning during standard growth conditions.

In the SAM, organs develop sequentially following a robust spatiotemporal organization, and vascularization is temporally decoupled from early organ growth, so water must necessarily travel from the vasculature through non-vascularized parenchymatic and meristematic cells[20]. In most aboveground plant tissues, water movement is

[1]Laboratoire de Reproduction et Développement des Plantes, Université de Lyon, ENS de Lyon, UCBL, INRAE, CNRS, INRIA 46 Allée d'Italie, 69364, Lyon, France. [2]Univ. Grenoble Alpes, CNRS, UMR 5525, VetAgro Sup, Grenoble INP, TIMC, Grenoble, France. [3]Present address: Organismal and Evolutionary Biology Research Programme, Faculty of Biological and Environmental Sciences and Viikki Plant Science Centre, University of Helsinki, Helsinki, Finland. [4]These authors contributed equally: Juan Alonso-Serra, Ibrahim Cheddadi. ✉e-mail: juan.alonsoserra@helsinki.fi; olivier.hamant@ens-lyon.fr

driven by stomata transpiration, but shoot meristems lack stomata, and water is expected to adapt to growing organs and fill them. Interestingly, growth per se has the capacity to lower the water potential, thereby attracting water, and it has been proposed as an additional driver of water movement in plants[21,22]. This is what we investigate here, taking advantage of the plant meristem as a model system.

First, we obtained a comprehensive map of volumetric growth of the SAM including developing organs up to stage 2 (before the flower organs appear) from Arabidopsis inflorescences. In addition to the expected differential growth rate between the organs and the meristem, we found evidence of cell shrinkage, specifically in the boundary domain. Using a modeling approach informed by our morphometric analysis, we predicted that higher growth rates in the organ may affect the hydraulic pattern and cause water deficit in the adjacent boundary tissue. The allocation pattern of a water-soluble dye was in agreement with our model and revealed a degree of symplasmic flow isolation in the boundary domain. This domain persisted even when the dye allocation was shifted to the apoplasm in ABA-deficient plants. Finally, by inducing de novo organ growth in intact meristems, we found further evidence of cell shrinkage adjacent to fast-growing cells.

Altogether, our study demonstrates that water is a factor whose non-uniform flux distribution contributes to the pattern of tissue development, in synergy with biochemical and mechanical cues.

Results

Global volumetric analysis of the SAM reveals shrinkage of deep boundary cells

Previous morphometric analyses of shoot meristems have revealed the cell volumetric growth dynamics of the CZ[23] or the initial stages of flower development[24]. Yet, these quantifications have not been related to water fluxes and have not been extended to later developmental stages with highly folded tissues. Growth and deformation rates of the area of the outer periclinal wall have been described for complete meristems of pimpernel, tomato, and Arabidopsis[25,26], but without volumetric insights. In order to understand the growth-driven hydraulic patterns in the whole SAM while considering tissue deformation, we measured cell volumetric changes along with tissue topology and changes in cell sphericity, during organ emergence. To do so, we performed time-lapse acquisitions using a plasma membrane marker and 3D watershed segmentation using timagetk tools (Fig. 1A and Supplementary Fig. 1; see "Methods").

The cell volume distribution was heterogenous with larger cells in developing organs and inner layers below the third layer of cells (L3) (Fig. 1B). The tissue surface mean curvature describes the topography of the meristem and serves as a morphological marker to identify the organ stage: organs in stage 1 do not exhibit a morphological crease at the boundary[27] whereas in stage 2-organs the saddle-shaped surface becomes significant (defined when the amplitude of the negative curvature is higher than that of the maximum curvature) (Fig. 1C). While cell sphericity and sphericity changes were variable in time and space, boundary cells were progressively deformed and became markedly least spherical in stage 2-organs (Fig. 1D, E). Then we quantified the volumetric changes, selecting cells that did not undergo division over 12 h. As expected, the younger organs and early boundary cells exhibited positive growth rates in this time window (Fig. 1F). In early boundaries, the mean curvature was positive and boundary cells, grew by 6.9 ± 3.8% while organ cells (stage 1) grew by 18.2 ± 6.8%. When the primordium reaches stage 2, the mean curvature becomes negative in the boundary. In this organ stage, more cell divisions were detected and cells had a higher volumetric growth rate (Fig. 1F). However, at later stages, i.e., three plastochrons after the transition to stage 2 (from primordium 5 (P5) onwards), we observed a new pattern at the boundary: cells localized either on the organ or on the PZ sides were expanding, while cells localized in the deep boundary domain were shrinking (Fig. 1F–H). This stage also coincided with a loss of sphericity in boundary cells. Yet, while many cells lost sphericity, only boundary cells shrank (Fig. 1I).

The shrinkage was of significant amplitude: shrinking cells lost on average 10.1 ± 4.6 % of their volume over 12 h, while the adjacent subpopulations (with negative mean curvature, too) exhibited a highly heterogenous expansion rate of 9.7 ± 9% on the organ side and 9.8 ± 8% on the PZ side. In the same time window, cells with positive mean curvature at the top of the organ grew by 19.9 ± 4 %, cells in the PZ by 6.1 ± 3 %, and CZ by 7.2 ± 3.3 %. This pattern was found in 6 meristems from 6 independent plants (Supplementary Fig. 2A). We also estimated the measurement error due to a different resolution in XY vs. Z. A multiangle analysis revealed an average of 0.3% error in volume estimation due to Z differential resolution (Supplementary Fig. 2B, C).

Including dividing cells in the growth map did not change the trend (Fig. 1G), consistent with the fact that cells in late boundaries rarely divide[28] and that most dividing cells contribute to organ and PZ expanding tissues. This analysis reveals that late boundary cells, despite being confined to a narrow space, can display opposing growth behaviors. A few of them lose volume without division, potentially revealing the consequences of growth-driven hydraulic patterns in the SAM.

Water efflux from the deep boundary domain is predicted by a mechano-hydraulic model

The above analysis suggests that boundary cells could experience a local water deficit as a consequence of the volume loss. This echoes a previous computational study[29], which suggested that, in theory, local tissue growth could induce water loss in cells surrounding the growing region. The model is a multicellular extension of the Lockhart-Ortega model[30](Fig. 2A–C). It assumes that every cell has a water potential composed of (i) a constant osmotic potential and (ii) a varying hydrostatic pressure. Water fluxes follow decreasing water potential; influx or efflux of water induces cell volume change (Fig. 2B), and mechanical constraints in cell walls accommodate for it (Fig. 2C). This, in turn, impacts the cell hydrostatic pressure (Fig. 2A), which creates a complex feedback loop between cell water potential, fluxes, and mechanical stresses in the cell. To explore the water loss hypothesis in our context, we adapted our 2D-multicellular model[29] to capture the key topological organization and growth rates of cells in a SAM section, including the central zone, peripheral zone, boundaries, and primordium (Fig. 2D, E).

The model parameters are adjusted such that L1, L2, and L3 cells are growing thanks to the water provided by cells underneath (Fig. 2D and Supplementary Table 1). The initiation of a primordium outgrowth ($t = 0$) is triggered by a decrease of the elastic modulus in the cell walls of the future organ (Fig. 2D). In the current model we adjusted the organ elastic modulus such that organ cells would grow 4 times faster than the rest of the tissue (Fig. 2E–G), as indicated by our morphometric measurements (see Fig. 1G). Simultaneously, wall deformation increases, and wall stresses and cell hydrostatic pressure decrease in the initiated organ (Fig. 2H and Fig. 3A, B). This local drop in pressure in the growing organ creates a water sink that draws water from neighboring cells (Fig. 3C). Water movement appears as an emerging property and fluxes are rapidly polarized to feed the growing organ. Hence, the boundary cells (indicated by red arrows in Fig. 3C) are caught between peripheral zone cells and organ cells, with limited access to water on one side and high demand on the other. In the first stage, they are hardly able to maintain positive growth. In the second stage, the water demand increases as the organ grows, up to the point where boundary cells begin to lose volume at a significant rate (Fig. 2F, G and Fig. 3D). During the simulation, boundary cells are progressively deformed (they lose sphericity), but this deformation does not always correlate with the volumetric changes highlighting the contribution of differential fluxes induced by neighboring cells (Fig. 2 I, J).

https://doi.org/10.1038/s41467-024-51099-x

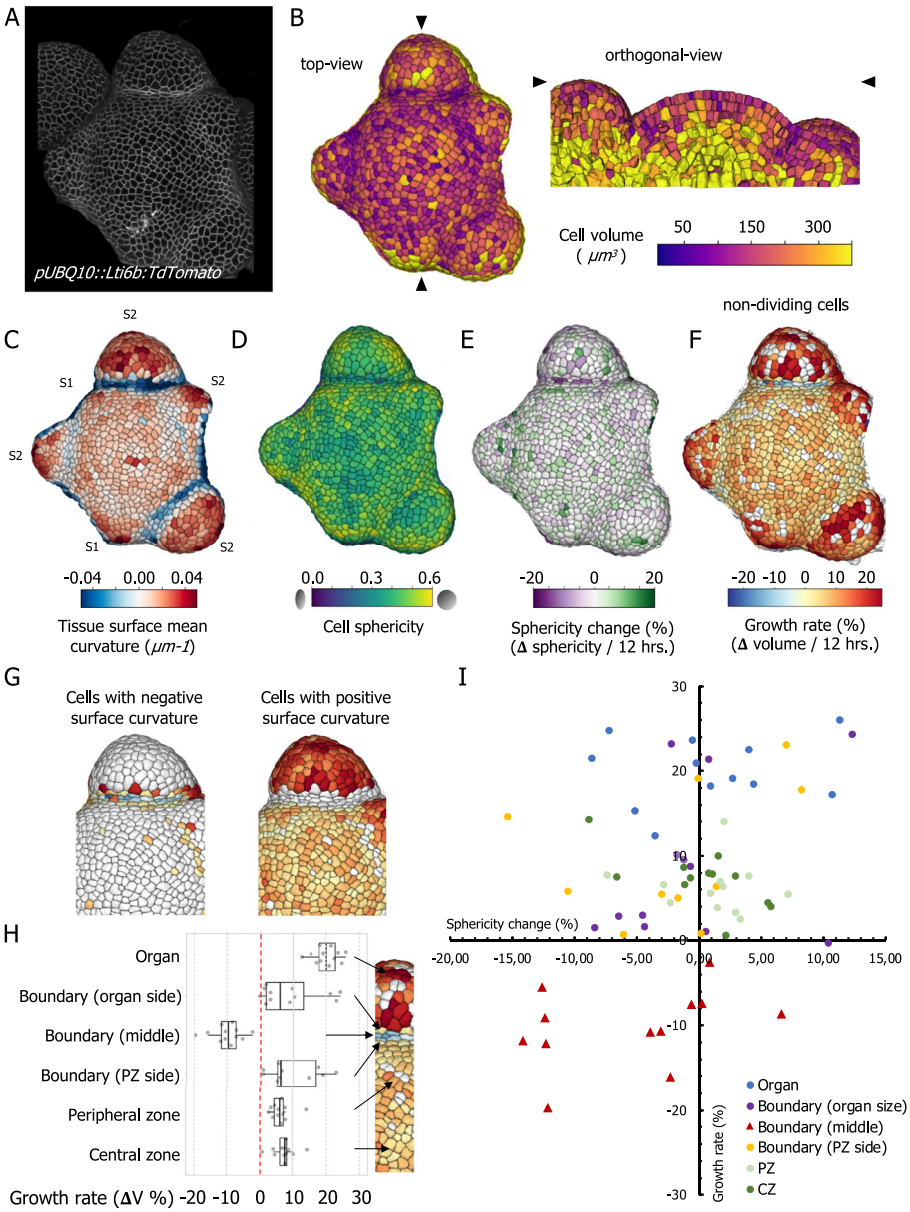

Fig. 1 | Morphometric analysis of the SAM reveals volumetric shrinkage at the deep boundary. A Processed signal of *pUBQ10::LTi6B-TdTomato* marker used for 3D segmentation (L1 only shown). **B** Heatmaps showing cell volumes from the top view (L1 only) and from an orthogonal view obtained at the site of the black arrows. **C** Heatmaps showing the surface mean curvature and the organ stages 1 (S1) and 2 (S2). **D** Heatmap showing cell sphericity. **E** Heatmap showing the sphericity changes over 12 h. **F** Heatmap showing volumetric growth rates over 12 h. Dividing cells appear in white, so growth rates are only shown for non-dividing cells. **G** Growth rate maps of a representative organ-meristem region including dividing cells (same sample as in panel **F**). The volume of daughter cells was added to obtain tissue-level growth rate. Note in panel (**F**) that no cell division was detected in the boundary. The subset of cells with negative curvature (left) and positive curvature (right). **H** Boxplot shows the position-dependent differential growth rates of cells for one meristem. The box indicates the interquartile range (IQR), the whiskers show the range of values within 1.5*IQR, and a horizontal line indicates the median. A similar heatmap profile was detected in all studied meristems ($n = 6$). **I** Scatter plot showing growth rate vs. sphericity change for cells quantified in (**H**).

To assess the robustness of this shrinkage effect in different growth conditions, we varied both the wall stiffness at the time of organ outgrowth (which affects growth rates) and the cell-to-cell water conductivity across L1L2L3 layers (Supplementary Fig. 3). Simulations resulted in different topography and growth rate dynamics of the primordium. Yet, the boundary-specific cell shrinkage was observed in all tested scenarios (Supplementary Fig. 3), suggesting that lateral water depletion is a robust emerging property of local primordium outgrowth.

A water-soluble dye does not reach the deep boundary domain

To get closer to causality, we would need to monitor water movements in our system. Water being, in essence, invisible under an optical microscope, its behavior can only be inferred with dyes, as a proxy for water movement. HPTS (8-hydroxypyrene 1,3,6 trisulfonic acid) is a membrane-impermeable, water-soluble dye, that has previously been used to reveal leaf-to-apex and cell-to-cell symplasmic transport in vegetative and inflorescence shoot apices[31]. Here we used a plasma membrane marker to resolve the anatomy in internal layers in the SAM and provided HPTS dye such that it would be acropetally transported from the stem (Supplementary Fig. 4A). Results presented below were obtained in 10 meristems from 10 independent plants.

After 1, 3, 6, 12, or 24 h of HPTS incubation, we detected a dye signal in the cytoplasm of meristematic cells (Fig. 4A, B and Supplementary Fig. 4B, C). However, pattern and signal intensity were more consistent

https://doi.org/10.1038/s41467-024-51099-x

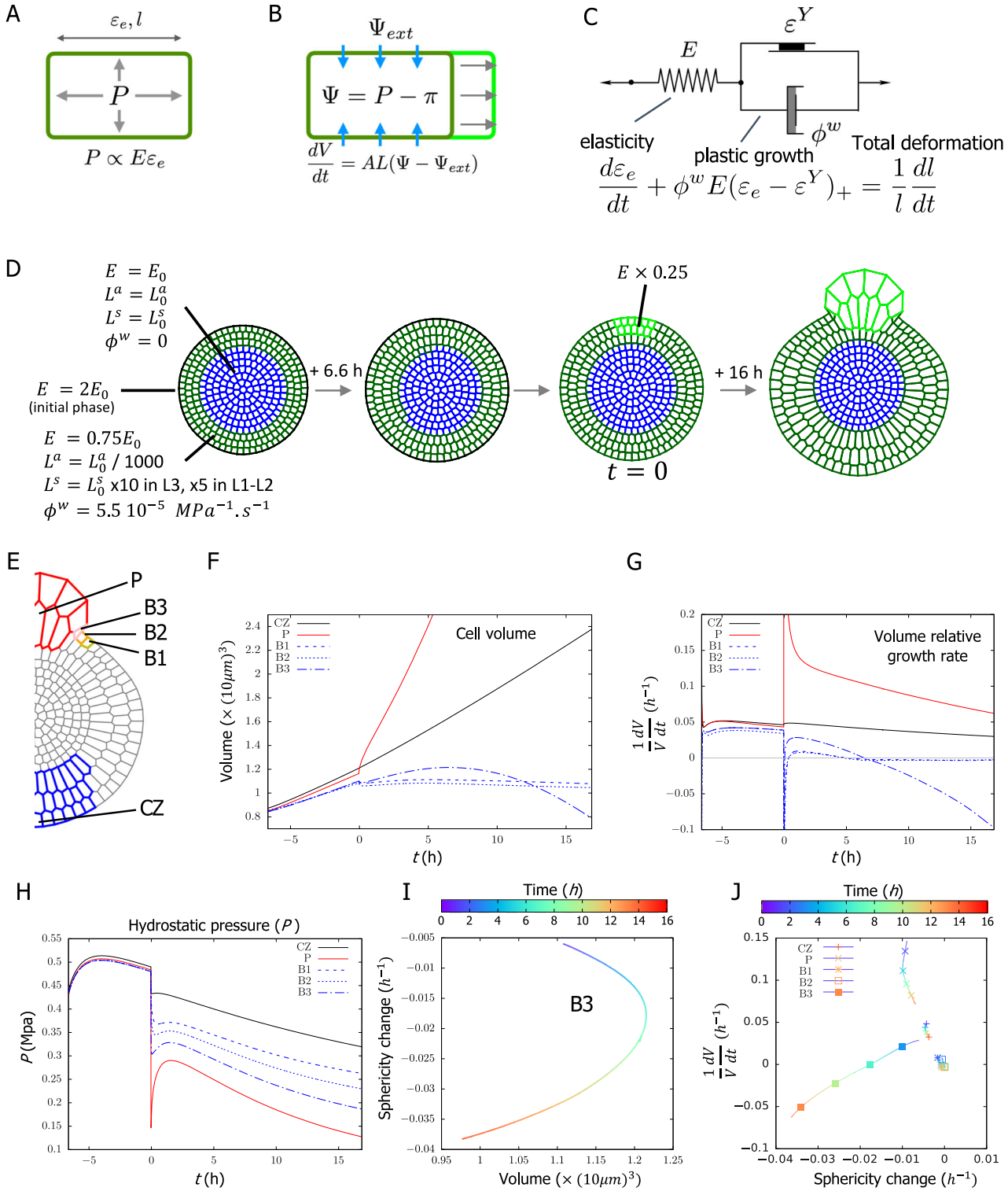

Fig. 2 | Parameter description of the model and time evolution of the reference simulation. A–C Lockhart-Ortega elongating single-cell model. **A** Cell pressure and wall tension equilibrate: pressure $\boldsymbol{P}$ is proportional to elastic modulus $\boldsymbol{E}$ and elastic deformation $\boldsymbol{\varepsilon_e}$. **B** Volume variation and water fluxes over surface $\boldsymbol{A}$ of permeability $\boldsymbol{L}$ depend on the difference between cell ($\boldsymbol{\Psi}$) and external ($\boldsymbol{\Psi_{ext}}$) water potentials. **C** Wall mechanical response decomposes into elastic (1st term on the left-hand side) and plastic (2nd term) responses; the plastic response corresponds to irreversible growth characterized by extensibility $\boldsymbol{\phi^w}$ and is triggered when the elastic deformation is above the threshold $\boldsymbol{\varepsilon^Y}$. The driving force is a large enough value of osmotic pressure $\boldsymbol{\pi}$ that induces water flux into the cell, which triggers simultaneously volume increase, wall deformation, pressure, and growth. **D** Scenario presented in the main text: initiation with a zero elastic deformation with regions defined by heterogeneous parameters (variables description in Supplementary Table 1); initial pressurization of the tissue; initiation of the primordium at $\boldsymbol{t = 0}$; growth of the primordium. **E** Regions where the time evolution is monitored: mean values over primordium cells (P) and central zone (CZ), individual cell values for the boundary cells (B1, B2 and B3). **F–H** Time evolution of cell volume (**F**), volume relative growth rate (**G**), and hydrostatic pressure (**H**). **I** Time evolution of boundary cell B3 (indicated in **E**) showing dynamics of sphericity change vs. volume. **J** Time evolution of selected cells (indicated in **E**) showing dynamics of volume relative growth rate vs. sphericity change. Time $\boldsymbol{t = 0}$ indicates the initiation of the primordium with a reduction of the elastic modulus.

https://doi.org/10.1038/s41467-024-51099-x

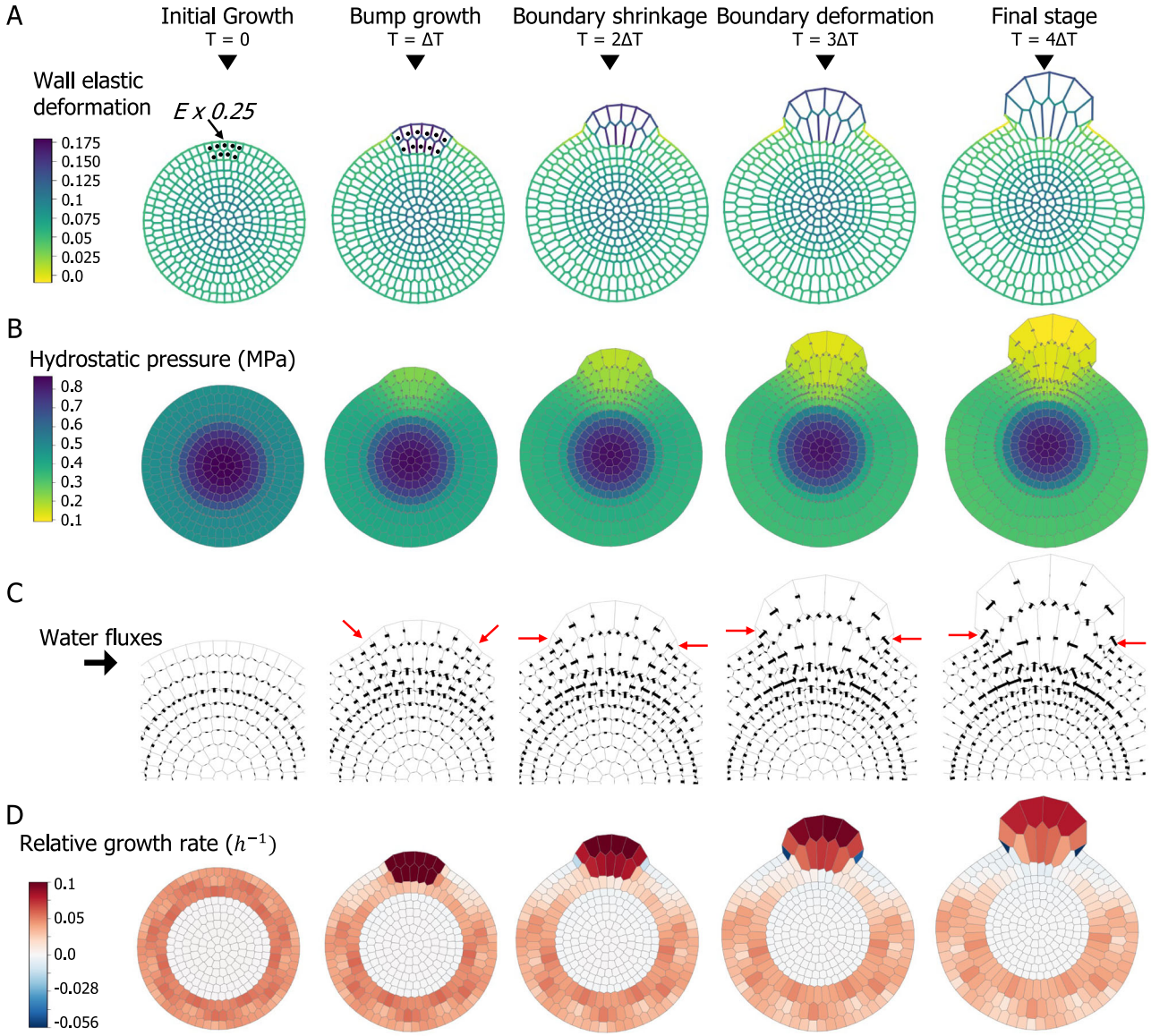

Fig. 3 | Vertex-based model of growth-derived water fluxes. A–D Multicellular model at regular intervals $\Delta T = 4.3\,h$, from the initial condition to the final stage: cells in the center deform elastically but cannot grow, they accumulate water from an external source and pressure; conversely, wall growth relaxes tension in cells in L1–L3; thanks to their lower pressure, they attract water from the center. **A** To mimic organ outgrowth, E is reduced (E x 0.25) in a subgroup of L1L2 cells (black dots) at time $T = 0$. **A–D** Maps of elastic deformation, hydrostatic pressure, fluxes, and relative growth rate; the boundary cells are indicated by red arrows in (**C**).

across samples after 6 and 12 h of incubation. After 6 h of incubation, and in line with a previous report[31], the HPTS signal was enriched in L1, L2, and L3 with a bias toward developing organs (Fig. 4C). A longer incubation time of 12 h further highlighted an organ-enriched pattern with HPTS dye being present in the cytoplasm and concentrated in vacuoles even in young developing primordia (P1 to P5) (Fig. 4B and Supplementary Fig. S4B). Furthermore, while longer HPTS incubation times of up to 24 h increased the overall signal intensity, the described pattern remained the same (Supplementary Fig. 4C). This pattern suggests that organs are indeed preferential sinks for symplasmic fluxes.

In order to characterize the earliest HPTS allocation pattern, we further quantified the HPTS signal after just 6 h of incubation. We detected a gradient of increasing HPTS intensity from the meristem to P5 stage organs (Fig. 4D). Strikingly, the boundary of advanced organs (P6–P7) displayed a marked drop in HPTS signal compared to the meristem or the organ, as viewed from the side or above (Fig. 4D–F and Supplementary Fig. 4D). Note that the signal of ubiquitously expressed plasma membrane marker did not exhibit such a pattern, indicating that the HPTS exclusion zone is not an optical artifact caused by tissue depth or curvature (Fig. 4F). Thus, HPTS is excluded from the boundary domain in that time period.

To check whether HPTS could ultimately reach the boundary domain, we monitored its distribution using increased resolution and correlative imaging with a membrane marker. After 12 h, HPTS accumulated in L2 and L3 of early-stage flower primordia (before bulging out) and flower organs (emerging outer sepal) (Supplementary Fig. 4E). We also observed an asymmetric signal distribution in stage 2 organs (e.g., P5–P7), with higher signal on the abaxial side, consistent with increased growth rate in that domain[24]. Yet, HPTS was still absent from the boundary domain (Supplementary Fig. 4E, white arrows).

To challenge our hypothesis of a growth-induced water loss in the boundary, we tested whether the observed patterns in that domain might instead primarily emerge from preestablished symplasmic communication pathways. ABA has been shown to regulate plasmodesmata-mediated symplasmic communication in shoot meristems of Arabidopsis, tomato, and poplar, and this mechanism is lost

https://doi.org/10.1038/s41467-024-51099-x

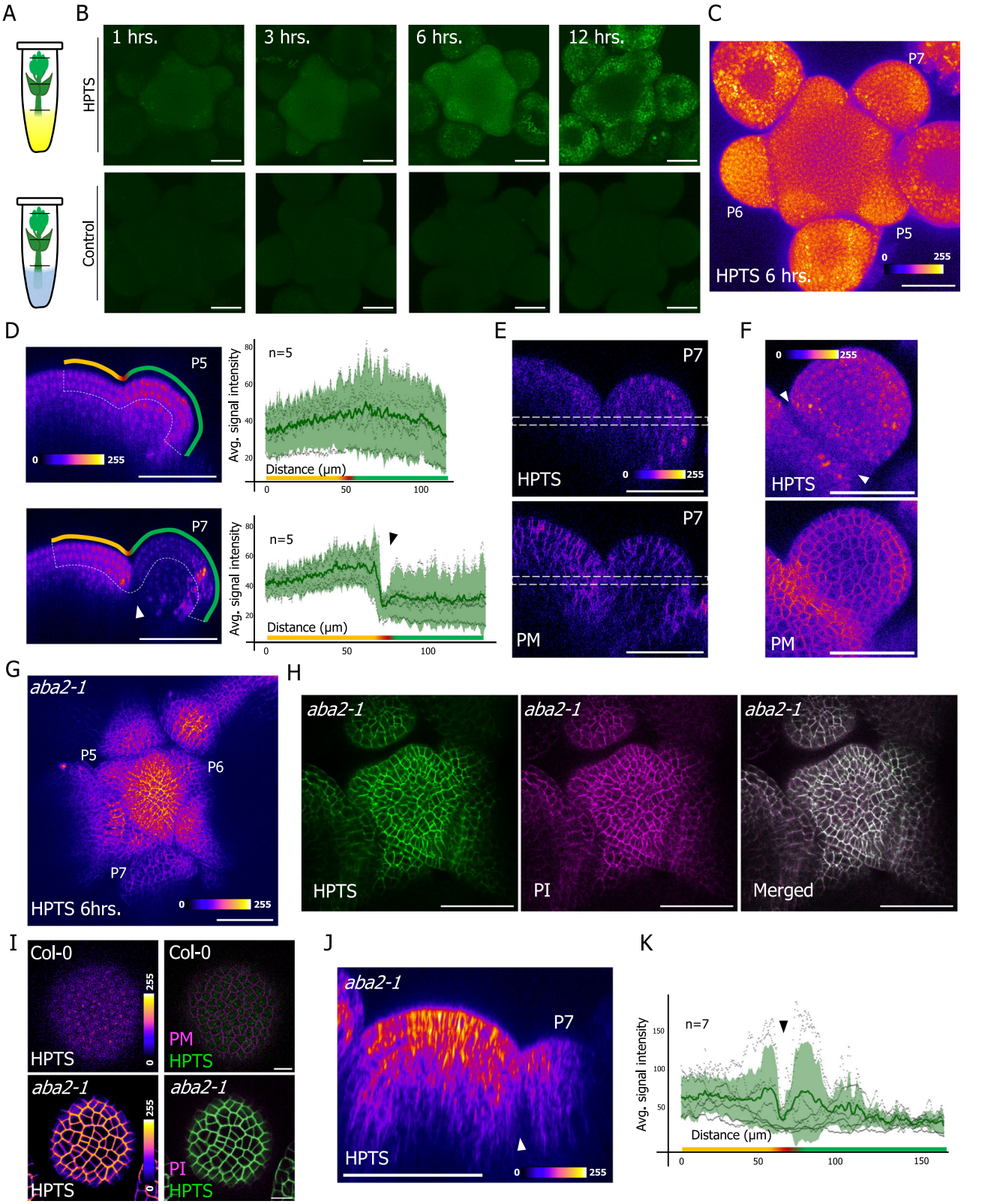

without ABA[18,19]. Therefore, we repeated the HPTS experiments using the ABA-deficient mutant *aba2-1*[32]. In this case, we detected HPTS primarily localized to the apoplast of meristematic and organ cells, colocalizing with propidium iodide which stains the cell walls and apoplast of living tissues (Fig. 4G, H). Unlike WT, the organ-enriched HPTS pattern was lost in the *aba2-1* mutant, and the dye distribution was broader, including the CZ ($n = 10$) (Fig. 4G, I and Supplementary Fig. S4F). However, when quantifying the HPTS signal across the meristem, we were still able to detect a domain with lower signal intensity coinciding with the boundary (Fig. 4J, K).

Whereas these results indicate that ABA has a major role in patterning symplasmic-apoplasmic pathways in the SAM, the water depletion domain at the boundary seems to emerge from an ABA-independent mechanism. This is consistent with a scenario where, at first order, the differential sink strength of organs creates a strong growth-induced water efflux at the boundary.

Fig. 4 | HPTS allocation patterns highlight the differential sink strength of organs. A Drawing showing the experimental setup. Shoot apices were treated by dipping stems in liquid ACM media with (top) or without HPTS (bottom). **B** HPTS (green) pattern after different incubation times in dissected meristems. Images are representative from $n = 5$, repeated twice. **C** Meristem obtained from the experiment shown in (**B**) showing a maximum intensity projection of HPTS pattern after 6 h of incubation. Organ stages P5, P6, and P7 are indicated. **D** Orthogonal sections illustrate the sampled layers (dashed white line in L1 and L2) of P5 and P7, after 6 h of dye incubation. For reference, meristem domains are indicated: top yellow line (CZ and PZ), red line (BZ), and green line (organ), see methods for sampling details. HPTS signal intensity profile plot showing the average (green line) and 95% confidence interval (light green) for L1L2 extracted from orthogonal sections ($n = 5$). **E** Orthogonal sections showing HPTS and plasma membrane (*pUBQ10::LTi6B-TdTomato*) signal intensities for P7 organs after 6 h of incubation. The white dotted lines define the limits of the stack of slices that were projected to obtain panel (**F**). Images are representative from $n = 5$, repeated twice. **F** Maximal projection of a 5 µm-thick transversal section in P7 organs showing HPTS and plasma membrane signal. **G** Maximum intensity projection of HPTS pattern of *aba2-1* after 6 h of incubation. Images are representative from $n = 5$, repeated twice. **H** Single meristem slice of *aba2-1* showing the HPTS, PI, and merged signals. **I** Close-up of CZ cells showing HPTS localization in Col-0 and *aba2-1* after 6 h of incubation. Images are representative of $n = 5$. **J** Orthogonal section of *aba2-1* after 6 h of incubation obtained as done in D for HPTS signal analysis. The white arrow indicates the boundary exclusion zone. **K** HPTS signal intensity profile plot showing the average (green line) and 95% confidence interval (light green) for L1L2 ($n = 7$). Data was obtained after 6 h of incubation. Heatmaps indicate the HPTS signal intensity. Scale bars = 50 µm. All experiments were independently reproduced at least once.

Differential growth rates generate cell shrinking domains in intact plants

In the previous experiments, shoot apices were cut from the stem, and most organs were removed to facilitate confocal imaging. To control for potential dissection-induced hydraulic artifacts on cell growth, we repeated the analysis using intact plants. To this end, we pre-treated in vitro-growing plants with N-1-naphthylphthalamic acid (NPA), which results in the development of pin-like shoot apices, fully accessible to optical microscopy. 48 h after transfer of the whole plant to an NPA-free medium, the meristem recovers and starts generating organs, allowing confocal access without organ dissection or stem cutting[33](see "Methods").

In this system, the growth rates were 4 to 6 times faster than in meristems from dissected shoot apices, thus requiring more frequent image acquisitions to capture the boundary formation. Tissue surface curvature and cell sphericity changes similar to those observed before were detected in just 2 to 4 h (Fig. 5A, B). The volumetric analysis revealed that organ cells grow by more than 20% (Fig. 5C, D). In agreement with our previous observations, we detected shrinking cells losing 7–10% of their volume in the midline and flanks of the newly formed boundary (Fig. 5C, D; $n = 6$). This confirms that a subpopulation of late boundary cells shrinks, consistent with predicted water efflux simulations, independent of dissection.

Strikingly, we also observed the presence of many epidermal cells shrinking below the meristem (Fig. 5D, G). Unlike cells in the midline boundary, the surface mean curvature for cells below the meristem was less pronounced or even positive, and not all of them showed loss of sphericity (Fig. 5E, F). This suggests that shrinkage could be more widespread than expected, especially in cells neighboring tissues with very fast growth.

If the negative growth of boundary cells is caused by water being pulled out by neighboring, fast-growing cells, then if growth were paused, the boundary cells should expand again. The higher temporal resolution in these meristems allowed us to test that hypothesis (Fig. 5G, H). Boundary cells that were originally shrinking during the first 2 h (T0 vs. T2) reversed this trend in the next 2 h (T2 vs. T4), revealing an elastic behavior (cells type 1 in Fig. 5G, H). For the same time window, adjacent cells (type 2) maintained their growth rate while cells on the rest of the organ (type 3) decreased their growth rate. These observations suggest that the shrinking at the boundary indeed anticorrelates with the growth rate at the organ.

More generally, since we systematically detected decreases in cell volume in boundary regions, both in dissected and non-dissected meristems, this supports the growth-driven water loss hypothesis in these cells.

A molecular signature of water loss at the boundary

Since the deep boundary is the site of water depletion, we expected to detect molecular signatures of water loss in that domain. Thus, we explored gene expression across different SAM domains using an available translatome from vegetative meristems[34], reasoning that a global molecular signature may provide indirect evidence of water loss. By performing a GO enrichment analysis on each subset of domain-specific upregulated genes, we found that genes associated with "abiotic and biotic stress" are enriched in the WUS, LAS, and PTL domains (Supplementary Data 1). The LAS domain, which best matches the early to late boundary domain, was differentially enriched for genes associated to "response to osmotic stress" and "response to salt stress" (Supplementary Fig. 5A). Examples of these are *RESPONSE TO DEHYDRATION 21B (RD21B)*, *EARLY-RESPONSIVE TO DEHYDRATION 8* (ERD8), *HAL3-LIKE PROTEIN A (HAL3)*, and *SIMILAR TO RCD1 (SRO5)*. This is consistent with local water depletion in that domain.

Next, we investigated whether a more generic marker of water loss could match the predicted water efflux at the boundary. In particular, modifications at the chromatin level have been associated with hyperosmotic stress in animals and in plants[35]. HISTONE 1.3 (H1.3) is a linker histone variant that has been reported to be drought-inducible[36,37]. It is also a marker of dormant bud set[38] and seed dormancy[39,40], i.e., in development processes that involve water loss. In inflorescence meristems, H1.3 has a patchy localization pattern in the CZ with a higher presence in the nuclei of deep boundary cells, i.e., in the crease between the emerging organ and the inflorescence meristem[11]. Using a protein fusion marker *pH1.3::H1.3-EGFP*[37], we confirmed this pattern (Fig. 6A, B).

To check whether H1.3 can mark other deep boundaries, we dissected vegetative meristems and found that in all meristems ($n = 9$), H1.3 was present in a few cells in the adaxial boundaries of rosette leaf primordia from P5 to at least P11 (Fig. 6C, D), but also in the boundary domain that surrounds axillary meristems (Supplementary Fig. 5B).

To control for dissection-induced stress, we repeated the analysis using intact pin-like shoot apices, from NPA-treated seedlings. In these conditions, H1.3 positive nuclei were observed exclusively in deep organ boundaries (Fig. 6E–G and Supplementary Fig. 5C). In order to check whether water loss can induce H1.3 in intact meristems, we further analyzed intact pin-like meristems under osmotic stress. Hypoosmotic conditions, through immersion in pure water, did not induce H1.3 in the pin-like meristem (Fig. 6H). However, treating plants with 300 mM mannitol (hyperosmotic conditions) induced H1.3 after 48 h. Strikingly, doubling the osmolyte concentration to 600 mM mannitol or sorbitol ($n = 7$) resulted in rapid H1.3 induction in just 8 h, with induction increasing further after 24 h of treatment (Fig. 6H and Supplementary Fig. 5D).

Altogether, we reveal that growth-derived water fluxes lead to volumetric shrinkage in deep boundaries near emerging organs at the shoot apex and define the geometry and molecular identity of that domain down to the chromatin signature.

Discussion

In essence, morphogenesis entails a change in shape and, thus, a change in structure, i.e., mechanics. In turn, mechanical stress,

https://doi.org/10.1038/s41467-024-51099-x

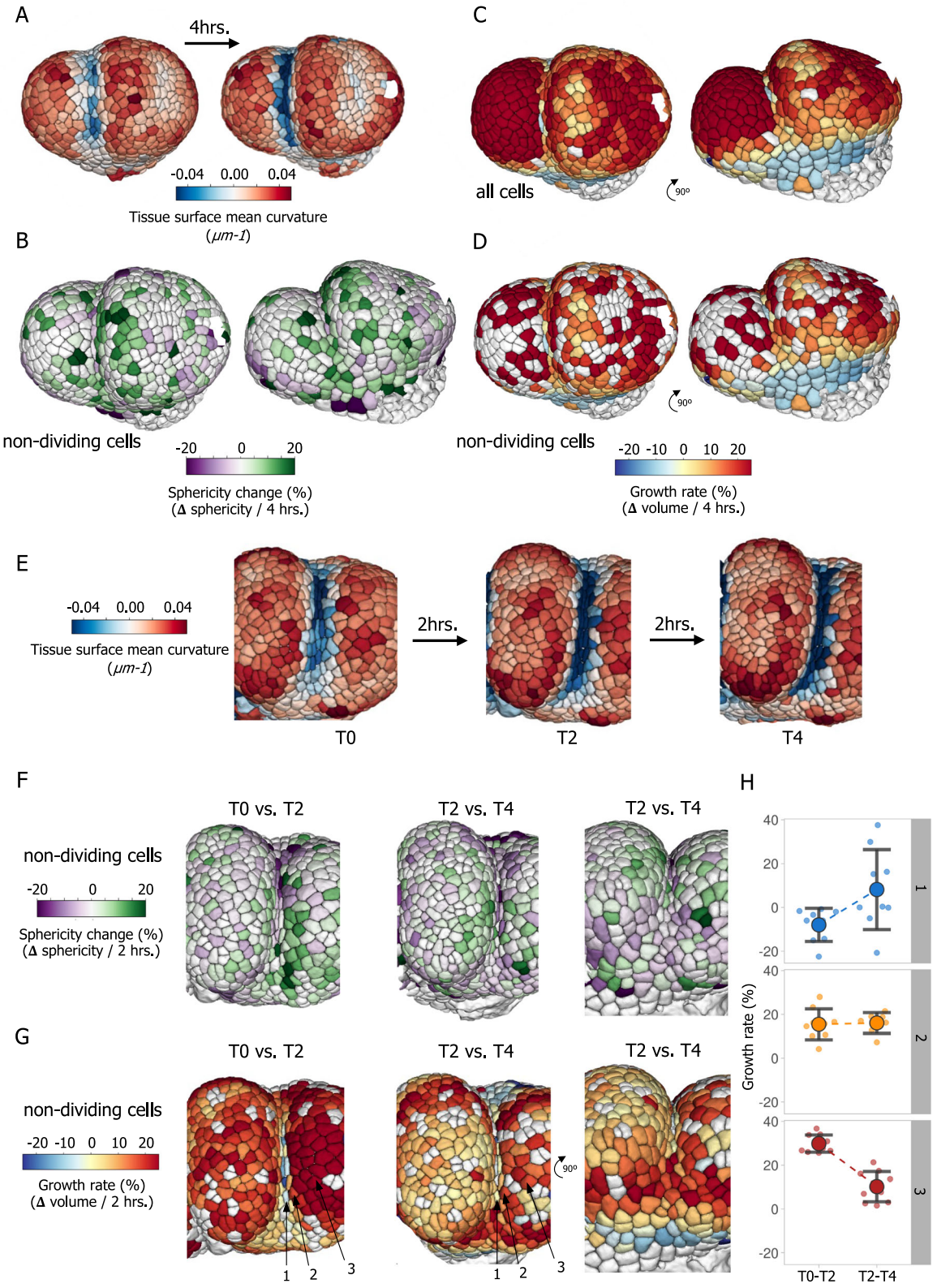

together with molecular patterning factors, controls morphogenesis. Here we propose that growth-induced deformation not only impacts the local stress pattern but it also affects the hydraulic pattern, which in turn helps to define boundaries. Growth-induced gradients of water potential, and therefore water movement, were proposed by Molz and Boyer[41], and since then described in elongating organs such as hypocotyls[21,42] and more recently in maize roots[22].

Note that one specificity of the shoot apex is that the water-draining role of the growing organ acts in synergy with tissue folding: the deep boundary cells are locked in a domain where tissue deformation geometrically restricts cell expansion. This might explain why differences in volumes are so significant in shrinking cells, and why these cells exhibit unusual behavior (reduced division rate[28], specific gene expression pattern[43]) and fate[44,45]. The deformation of boundary

Fig. 5 | Negative growth is observed in deep boundaries from intact (non-dissected) pin-like shoot apices. A Early organ outgrowth heatmap showing the surface curvature before and after 4 h. **B** Heatmap showing the cell sphericity changes during the same 4 h. of growth. **C** Heatmaps represent the volumetric growth rates including cell divisions (**C**) or marking dividing cells in white (**D**). The same samples were rotated 90° to visualize shrinking cells detected at the boundary flanking sides. **E** Three time points show the developmental progression of an advanced boundary with heatmaps representing the surface mean curvature (**E**), and the corresponding cell sphericity changes (**F**) and volumetric growth rates (**G**) for non-dividing cells. Note the presence of pale blue cells, i.e., shrinking cells, in the deep boundary (left image) and below the meristem (right image). Cell types 1 (shrinking cell), 2 (adjacent to shrinking cell), and 3 (non-adjacent organ cells) are identified in T0–T2 and T2–T4. **H** Growth rates for cell types 1 ($n = 9$), 2 ($n = 8$), and 3 ($n = 10$) at T0–T2 and T2–T4 originating from the same meristem shown in (**G**). Large dots indicate the mean, and black lines represent the standard deviation.

cells has been previously modeled as compression between the organ and the meristem[8], a domain where even cell nuclei are progressively deformed[11]. Our measurements in vivo and modeling suggest that the cell shrinkage observed at P5 precedes this process. First, loss of cell sphericity (as a proxy for cell deformation) does not always result in volumetric shrinkage, and a few boundary cells at P5 shrink without losing sphericity (Fig. 1I). Secondly, the cell wall stiffness and turgor pressure of emerging organs are expected to be lower compared to neighboring tissues, indicating that P5 organs are less likely to push against the meristem (Fig. 3B and[46]). However, cell deformation and further cell shrinkage by compression of boundary cells may occur immediately after, from P6 or P7 onwards, when the faster abaxial growth bends the organs against the meristem. Such compression would still act in synergy with the water drainage at the boundary facilitated by the differential growth at the organ.

In addition to growth, hydraulic patterns across tissues are also shaped by the degree of tissue interconnection and the osmotic pressure (e.g., osmolyte concentration) of different cell types. Therefore, while the HPTS allocation pattern we described fits a growth-induced model, we do not exclude the contribution of other factors. In terms of tissue interconnection, plasmodesmata (PD) and aquaporins offer a path for water movement through the symplasmic and symplasmic-apoplasmic domains, respectively. PD connections are controlled by ABA in roots[16] and shoots[18,19] where an ABA increase leads to PD closure. The surprising finding that HPTS is enriched in the apoplast in ABA-deficient plants (Fig. 4) suggests that in this context cells cannot retain the dye. Since ABA also regulates water loss[32], cuticle biosynthesis[47], xylem differentiation[48], and aquaporin function[49], a more complex hydraulic picture may emerge in ABA-deficient plants. Interestingly, the HPTS allocation pattern is more homogenous across SAM domains in *aba2-1*, indicating that when the apoplasmic path is favored, dye movement is less restricted. Yet, despite the significant changes in the dye allocation pattern, the boundary exclusion zone was still present in *aba2-1*. Meristems are smaller in *aba2-1* (Fig. 4G) indicating that overall growth is affected. Yet, organs still grow which, together with the CZ, act as sinks, and the dye is excluded from the boundary domain. Such observation supports the hypothesis that tissue growth domains prescribe water allocation patterns regardless of the transport path, symplasmic or apoplasmic. Additional studies are required to determine the contribution of the osmotic pressure and aquaporins to the observed pattern. Among the boundary-upregulated genes, we identified two candidates that could contribute to water potential at the boundary: the vacuole-localized aquaporin *TONOPLAST INTRINSIC PROTEIN (TIP3.1)*[50] and *OUTER MEMBRANE TRYPTOPHAN-RICH SENSORY PROTEIN (TSPO)*. TSPO is involved in the posttranslational regulation of PIP2;7, a plasma membrane-localized aquaporin also expressed in the SAM[51]. Similar to other boundary genes, both *TIP3.1* and *TSPO* are upregulated by osmotic stress.

Even in narrow domains of the SAM, hydraulic properties such as turgor pressure are heterogeneous and depend e.g., on tissue topology[52]. Our complementary finding of shrinking domains next to fast-growing sectors supports the long-proposed hypothesis of growth-induced water potentials and water transport across the tissue[21]. Thus, late boundaries shrinkage is partly a hydraulic consequence of organ outgrowth, which contributes to the final tissue topography. This makes water a patterning factor at the shoot apex acting in synergy with mechanical and biochemical cues.

Taken together, our results open a new avenue of research on the role of water flux as an instructive factor in patterning cell identity in meristems and beyond. While the example of the deep boundary may appear as an extreme case due to strong tissue curvature, we believe that such shrinkage might be more widespread. In this work, we could observe this effect in the region below the growing organs in non-dissected shoot apices. Such water fluxes may, in turn, have many impacts on patterning tissue growth and identity. For instance, it has recently been shown that the inhibition of lateral roots during xero-branching response to dry soil, is controlled by a change in internal fluxes that reshapes hormonal gradients[16]. It is thus possible that, despite being less detectable, water fluxes contribute to the patterning of many more tissues in plants, and likely in other kingdoms too. For instance, osmolarity can impact membrane tension and cell polarity, with shared mechanisms between plants and animals[53]. One could imagine that water fluxes also contribute to tissue patterning in animal embryos, with a similar impact on gene expression and chromatin signatures.

Methods

Plant materials and growth conditions

Plasma membrane marker *pUBQ10::LTi6B-TdTomato* and the protein fusion marker *pH1.3::H1.3-EGFP* have been previously generated[37,54]. *aba2-1* mutant was previously described[32]. Dissected meristems and naked meristems (without organs) were obtained and processed as previously described[33]. Briefly, two protocols were used to image-shoot apical meristems:

(i) For analysis of reproductive meristems, plants were grown on soil for 4 weeks under long-day (16 h light / 8 h dark) conditions. Reproductive meristems were dissected right after bolting when the stem was 1-2 cm. After dissection reproductive meristems were transferred to the previously described apex culture medium (ACM) supplemented with N6-benzyladenine (500 nM)[33]. Shoot apices were kept in a long day chamber until and during imaging. To reveal the apoplastic HPTS allocation in *aba2-1* meristems were additionally stained using propidium iodide.

(ii) Naked meristems were obtained by growing sterilized seeds in Arabidopsis media containing 10 µM of NPA (N-1-Naphthylphthalamic Acid) (Sigma) as previously described[33], pin-like meristems emerged after 3 to 4 weeks depending on the line. The plants were then transferred to an NPA-free medium to induce organ outgrowth (most experiments) or left on an NPA medium to maintain a naked meristem.

HPTS incubation experiments

Inflorescence meristems from long day grown plants were used in all HPTS incubations. After bolting, 5 cm - tall stems were cut at the base and immediately transferred to an Eppendorf tube containing liquid ACM (without agarose) supplemented with 2.5 mg/mL of HPTS (Molecular Probes, Leiden, Netherlands). Tubes for control samples contained only liquid ACM. Stems were then incubated in a humid chamber (i.e., saturated hygrometry with a wet paper) under long-day conditions for 1 ($n = 5$), 3 ($n = 5$), 6 ($n = 10$), 12 ($n = 10$), and 24 h ($n = 5$). Stems were dissected right after the incubation time and placed in a Petri dish with solid ACM for imaging within the following 30 minutes. In order to obtained the profile of HPTS signal intensity in L1 and L2, we

https://doi.org/10.1038/s41467-024-51099-x

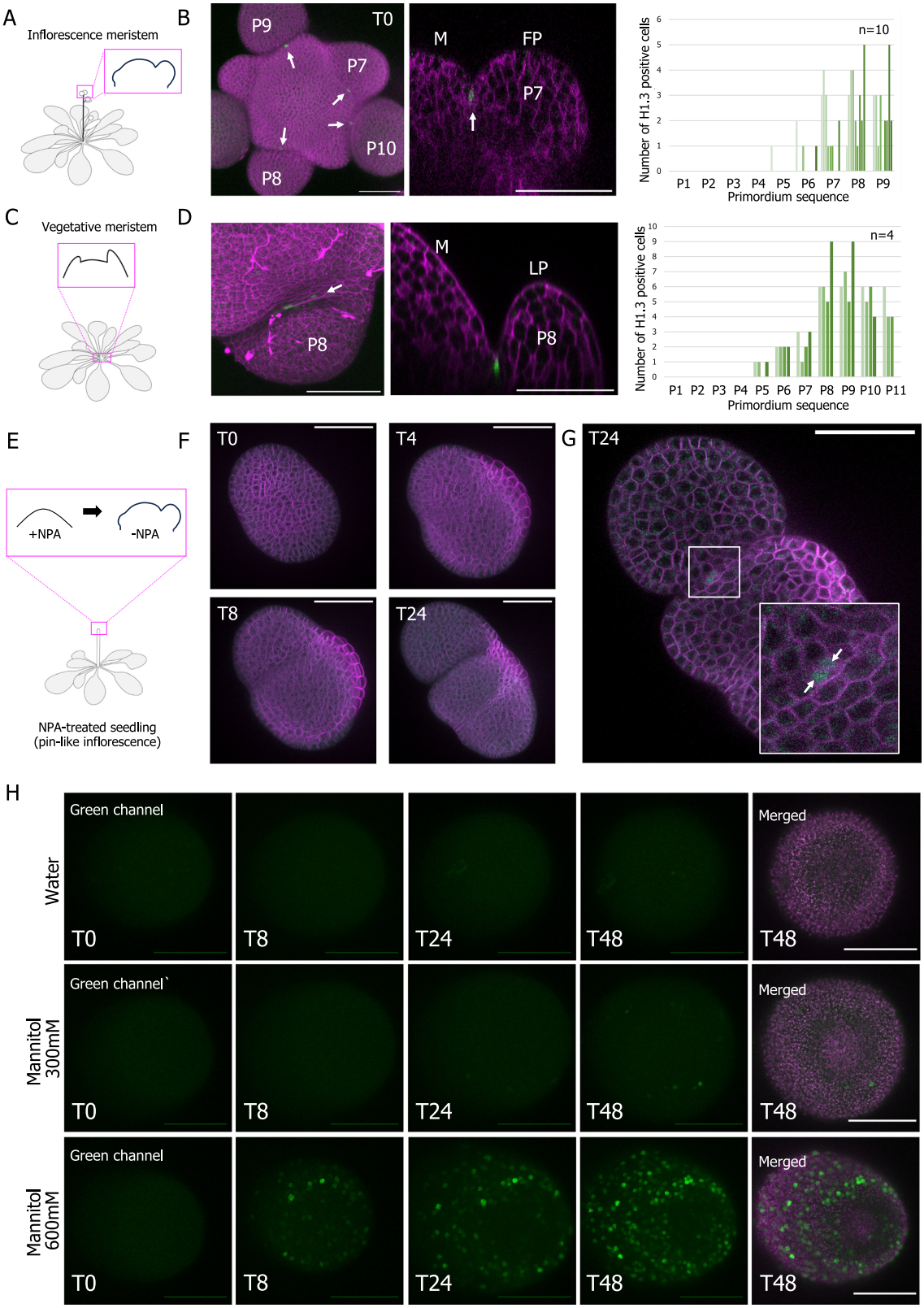

used ImageJ (Z project plugin) to generate maximum intensity projections of 10 µm thick orthogonal image stack of different primordium stages (P5 and P7). Next, a region of interest was selected using a line (10 µm thick) that covers the L1 and L2 cell layers from the central zone to the abaxial side of primordium. Signal intensity levels for 5 meristems from 5 independent plants were then plotted using the online tool Plot of Twist (https://huygens.science.uva.nl/PlotTwist/). HPTS experiments with NPA-induced pin-like meristems were not possible because root or leaf-provided HPTS failed to reach the shoot apex.

Model description

We built an abstract bidimensional multicellular description of a SAM in the framework of the so-called vertex-based models[55] where pressure in the cells equilibrates with tension in the walls. As in the Lockhart model[56], this mechanical equilibrium is coupled to the growth of

Fig. 6 | Late boundaries are labeled by water stress marker histone H1.3. **A** Inflorescence meristem localization. **B** Pattern of *pH1.3::H1.3-GFP* localization (green) right after dissection: maximum intensity projections (left), orthogonal section of the same image stack (middle), and number of H1.3 positive cells at the boundary of each primordium stage (right). **C** Vegetative meristem localization. **D** Pattern of *pH1.3::H1.3-GFP* localization (green) right after dissection: maximum intensity projections (left), orthogonal section of the same image stack (middle), and number of H1.3 positive cells at the boundary of each primordium stage (right). **E**–**G** Time series of new organs growing out of a non-dissected pin-like meristem 2 days after transferring to NPA-free medium at T0, T4, T8, and T24 hours. (G) Magnified transversal section of the T24 with inset showing 2 cells with H1.3 positive nuclei at the boundary. Representative images of $n = 5$, repeated at least once. M, meristem, LP, leaf primordium, FP, flower primordium. White arrows indicate H1.3 positive cell nuclei. Magenta corresponds to PI staining (**B**) or the plasma membrane marker *pUBQ10::LTi6B-TdTomato* (**D**, **F**, **G**). **H** Maximum intensity projections of pin-like meristems showing the temporal H1.3 inducibility after mannitol. Hyperosmotic stress evoked by mannitol treatment (300 mM) induced H1.3 after 48 h ($n = 5$), while induction was observed as early as 8 h after treatment with mannitol 600 mM ($n = 5$). No induction was observed in the hypoosmotic treatment (controls). The green channel shows *pH1.3::H1.3:GFP,* and magenta corresponds to chlorophyll. Scale bars = 50 µm.

the walls and to osmosis-based water fluxes between cells and between cells and water sources.

Mechanical equilibrium: Let P_i be the turgor pressure in each cell i, ε_k^e the elastic deformation of each wall k, and E_k its elastic modulus ($\sigma_k = E_k\varepsilon_k^e$ is then the mechanical stress). The tissue being at every moment in quasi-static equilibrium, pressure forces on wall edges and elastic forces within walls balance exactly; in a vertex-based model, this leads to, at each vertex v:

$$\frac{1}{2}\sum_{k\sim v}\Delta_k P A_k \boldsymbol{n}_k + \sum_{k\sim v} E_k\varepsilon_k^e a_k \boldsymbol{e}_{k,v} = 0 \quad (1)$$

Where the sums are computed over the indices of walls $k \sim v$ adjacent to vertex v, and $\Delta_k P = P_{k_1} - P_{k_2}$ is the pressure jump across wall face k, $k_1 < k_2$ are the indices of the cells separated by face k, A_k is the area of the face k on which pressure is exerted, $\boldsymbol{n}_k$ is the normal vector to face k, oriented from cell k_1 to cell k_2, a_k is the cross-section of the face, on which the elastic stress is exerted, and, finally, $\boldsymbol{e}_{k,v}$ is the unit vector in the direction of face k, oriented from vertex v to the other end of face k. In the case of the geometry of the Lockhart model, this mechanical equilibrium leads to a constant proportionality between pressure and wall deformation, but in the more general case here, the relation between pressure and wall deformation depends on the varying geometry of the cells.

Cell wall growth: The cell walls are modeled as a visco-elasto-plastic material, similarly to the Ortega model[30]. Let l_k be the length of wall k, the rate of change of ε_k^e is given by:

$$\frac{d\varepsilon_k^e}{dt} + \phi_k^w E_k(\varepsilon_k^e - \varepsilon_k^Y)_+ = \frac{1}{l_k}\frac{dl_k}{dt} \quad (2)$$

Where ϕ_k^w is the extensibility and ε_k^Y is the yield deformation of wall k, and $(x)_+$ is the positive part of any real number x. This equation describes the fact that a wall k with an elongation rate $\frac{1}{l_k}dl_k/dt$ (*e.g.,* because of an influx of water) will develop an elastic deformation and therefore, tension, and that growth will relax any elastic deformation above the threshold ε_k^Y with a characteristic time $1/(\phi_k^w E_k)$.

Water fluxes: In the context of plant tissues[57], the water potential reduces to $\Psi = P - \pi$, where π is the osmotic pressure. As in the Lockhart model, fluxes across a perfectly semi-permeable membrane of surface A and permeability L follow decreasing water potential gradients and are in the form $U = AL\Delta\Psi$. In the model presented here, cells can exchange water between them and with the apoplasm, which is assumed to have a constant water potential $\Psi^a = 0$, and behaves as a water supply for the growth of the cells. In addition, we assume that water fluxes account for all the volume variations of the cells, and we get, for each cell i:

$$\frac{dV_i}{dt} = A_i L_i^a(\Psi_i - \Psi^a) + \sum_{j\sim i} A_{ij}L_{ij}^s(\Psi_j - \Psi_i) \quad (3)$$

Where A_i is the surface of the cell i, L_i^a its permeability with the apoplasm, Ψ_i its water potential; the sum is performed over the neighbor cells $j \sim i$ adjacent to the cell i, and A_{ij} is the common surface between cells i and j, and L_{ij}^s the water permeability. For parsimony, the osmotic pressure is assumed constant and homogeneous in the cells.

The coupling between these three equations results in a complex mathematical and computational problem for which we provided a numerical resolution in ref. 29. Pressure and growth rate are not prescribed in this model, as they emerge from the interaction between fluxes and wall rheology, through the mechanical equilibrium. This model has already been quantitatively compared to biological data and predicted pressure and growth rate heterogeneities in the SAM[52].

Simulations presented in this article: The goal here is to represent the differential growth between organs and the central zone in the SAM (Fig. 2), with water supplied from below. In order to avoid boundary conditions between the SAM and the tissue underneath, we choose an initial circular geometry with 316 cells organized in concentric layers (Fig. 2D). This bidimensional mesh can be interpreted as a section through the SAM along the axis of the stem. Then, the identity of the cells is determined by the choice of the parameters of the model (Fig. 2D and Supplementary Table 1). Cells in the center, below L3, do not grow ($\phi^w = 0$) and are connected to a water source ($L^a \neq 0$), they mimic the basal part of the SAM that is connected to vascular bundles providing water. Conversely, cells in L1–L3 layers are isolated from the water source (L^a is three orders of magnitude lower) and grow thanks to the water from cells below; water mostly travels from cell to cell in L1–L3, which implies that they are in competition for water. The elastic modulus is 75% of cells below in L1–L3 and 200% in the outer wall in the initial growing phase. Starting from an initial state with zero elastic deformation, the tissue is put under pressure until the center cells have reached a stationary pressure, and cells in L1–L3 have started their plastic growth. This state is reached after 6.64 h in the simulation, and this marks the time $t = 0$. The detailed values of the parameters are given in Fig. 2D and Supplementary Table S1. The outgrowth of the primordium is then triggered by a further decrease of the elastic modulus in a few cells in L1–L3 (x 0.25 in the reference simulation, x 0.5, and x 0.75 in the parameter exploration below, Supplementary Fig. 3).

This abrupt decrease of the elastic modulus induces 1) a global drop of the pressure (Fig. 2H and Fig. 3B), especially in the primordium, and 2) a peak in the growth rate of the primordium and a drop in the boundary cells B1, B2, B3 (Fig. 2F, G and Fig. 3D). This initial fast response corresponds to transient elastic response, and after ≈ 1 h the cells have adapted to the change of conditions. As explained in the main text, the boundary cells B3 end up losing water to the primordium. Note that this shrinkage is not due to compression as the pressure in the primordia is lower than the pressure in the boundary. The pressure and growth rate are globally decreasing with time, as an effect of the global increase of cell volume, as analyzed in ref. 29. One can also notice an apparently periodic growth rate heterogeneity in the region far from the primordium, this is due to a topology (number of neighbors) heterogeneity in the construction of the mesh, as analyzed in ref. 52.

Image analysis

Image acquisitions. All confocal acquisitions were performed using a Leica SP8 or a Zeiss LSM980 microscope. A SP8 microscope with a

resonant scanner was used for the time-lapse acquisitions on dissected meristems and pin-like meristems were imaged with Zeiss LSM980.

Volumetric analysis. In order to improve the quality of the plasma membrane marker signal, all confocal stacks were resampled to get isometric voxels and then processed by an anisotropic diffusion filter[52]. Then, to increase the signal level in the outer periclinal membranes of the epidermal cell layer, we used a Level Set Method to locate the tissue surface precisely[58] and added the obtained contour to the original image (Supplementary Fig. 1A). This step was particularly important to accurately delimit cells in the boundary region of the meristem.

Then we performed an automated 3D seeded watershed segmentation derived from the MARS algorithm[59] and obtained a 3D labeled image stack (Supplementary Fig. 1B). Using the Blockmatching method[60], we registered the membrane marker images of consecutive time points to obtain the 3D vector field deforming the tissue at T0 onto the one a T0 + T. We applied this geometrical transformation to the segmented image at T0, and automatically extracted the cell lineages by identifying the most overlapping cells between T0 and T0 + T. These cell lineages allowed us to directly evidence new cell divisions (Supplementary Fig. 1C). We used the implementations of the segmentation and registration algorithms provided in the Tissue Image ToolKit Python library (https://mosaic.gitlabpages.inria.fr/timagetk).

We quantified morphological cell properties, such as cell volumes, directly on the 3D labeled image. Then, to estimate the mean curvature at the level of epidermal cells (Supplementary Fig. 1D), we extracted a triangle mesh of the tissue surface, using decimation and smoothing on the mesh obtained by applying the Marching Cubes method on the binary mask of the segmented image. The surface mesh extraction was performed using the implementations provided in the VTK library[61]. We computed the principal curvatures at the level of each triangle of this mesh based on the vertex normal vectors[62] and averaged this information on the mesh vertices (area-weighted average of incident triangles). The mean curvature of the tissue surface at the level of a given epidermal cell was then estimated as the mean curvature at the vertex of the surface mesh that lies closest to its center. Cell sphericity was calculated using the following formula: Sphericity = $36\ \pi\ {}^*V^2/S^3$, where V is the cell volume and S is the total cell surface.

Automated scripts performing these successive image analysis steps, as well as visualization of the output segmentations and quantified properties, were made available in the titk_tools Python package (https://gitlab.inria.fr/gcerutti/boundary_registration).

Since the XY resolution (ca. 200 nm) in our images was different from that in the Z orientation (ca. 500 nm), we aimed at identifying the error in volumetric measurements by comparing multiangle acquisitions in pin-like meristems. To do so, we imaged meristems first in the standard vertical position (VP1), then in a tilted angle of 30° (TA), and finally in the vertical position again (VP2). The time between confocal acquisitions was less than 2 minutes. The error associated to consecutive confocal imaging (VP2 -VP1) was 5.5 ± 3%. The error associated with the Z distortion (VP1-TA) − (VP1-VP2) = 0.27 ± 5%.

All box plots were generated using the online tool Plots of Data (https://huygens.science.uva.nl/PlotsOfData/).

Reporting summary

Further information on research design is available in the Nature Portfolio Reporting Summary linked to this article.

Data availability

All raw images used for segmentation in this study have been deposited with unrestricted access at https://figshare.com/s/728ab7c68bb98160352d (https://doi.org/10.6084/m9.figshare.25790457). Other materials or data are available on demand and/or in the main text and supplementary material.

Code availability

All code associated with the current submission is available at https://figshare.com/s/728ab7c68bb98160352d (https://doi.org/10.6084/m9.figshare.25790457).

References

1. Lecuit, T., Lenne, P.-F. & Munro, E. Force generation, transmission, and integration during cell and tissue morphogenesis. *Annu. Rev. Cell Dev. Biol.* **27**, 157–184 (2011).
2. Hayward, M.-K., Muncie, J. M. & Weaver, V. M. Tissue mechanics in stem cell fate, development, and cancer. *Dev. Cell* **56**, 1833–1847 (2021).
3. Godard, B. G. & Heisenberg, C.-P. Cell division and tissue mechanics. *Curr. Opin. Cell Biol.* **60**, 114–120 (2019).
4. Mammoto, T., Mammoto, A. & Ingber, D. E. Mechanobiology and developmental control. *Annu. Rev. Cell Dev. Biol.* **29**, 27–61 (2013).
5. Hamant, O. & Saunders, T. E. Shaping organs: Shared structural principles across kingdoms. *Annu. Rev. Cell Dev. Biol.* **36**, 385–410 (2020).
6. Echevin, E. et al. Growth and biomechanics of shoot organs. *J. Exp. Bot.* **70**, 3573–3585 (2019).
7. Trinh, D.-C. et al. How mechanical forces shape plant organs. *Curr. Biol.* **31**, R143–R159 (2021).
8. Hamant, O. et al. Developmental patterning by mechanical signals in Arabidopsis. *Science* **322**, 1650–1655 (2008).
9. Nakayama, N. et al. Mechanical regulation of auxin-mediated growth. *Curr. Biol.* **22**, 1468–1476 (2012).
10. Heisler, M. G. et al. Alignment between PIN1 polarity and microtubule orientation in the shoot apical meristem reveals a tight coupling between morphogenesis and auxin transport. *PLoS Biol.* **8**, e1000516 (2010).
11. Fal, K. et al. Tissue folding at the organ-meristem boundary results in nuclear compression and chromatin compaction. *Proc. Natl. Acad. Sci. USA* **118**, e2017859118 (2021).
12. Landrein, B. et al. Mechanical stress contributes to the expression of the STM homeobox gene in Arabidopsis shoot meristems. *Elife* **4**, e07811 (2015).
13. Weits, D. A. et al. An apical hypoxic niche sets the pace of shoot meristem activity. *Nature* **569**, 714–717 (2019).
14. Dinneny, J. R. Developmental responses to water and salinity in root systems. *Annu. Rev. Cell Dev. Biol.* **35**, 239–257 (2019).
15. von Wangenheim, D. et al. Early developmental plasticity of lateral roots in response to asymmetric water availability. *Nat. Plants* **6**, 73–77 (2020).
16. Mehra, P. et al. Hydraulic flux–responsive hormone redistribution determines root branching. *Science* **378**, 762–768 (2022).
17. Péret, B. et al. Auxin regulates aquaporin function to facilitate lateral root emergence. *Nat. Cell Biol.* **14**, 991–998 (2012).
18. Wu, Y. et al. Abscisic acid employs NRP-dependent PIN2 vacuolar degradation to suppress auxin-mediated primary root elongation in *Arabidopsis*. *N. Phytol.* **233**, 297–312 (2022).
19. Tylewicz, S. et al. Photoperiodic control of seasonal growth is mediated by ABA acting on cell-cell communication. *Science* **360**, 212–215 (2018).
20. Dengler, N. G. The shoot apical meristem and development of vascular architectureThis review is one of a selection of papers published on the Special Theme of Shoot Apical Meristems. *Can. J. Bot.* **84**, 1660–1671 (2006).
21. Boyer, J. S. Cell enlargement and growth-induced water potentials. *Physiol. Plant* **73**, 311–316 (1988).
22. Robbins, N. E. & Dinneny, J. R. Growth is required for perception of water availability to pattern root branches in plants. *Proc. Natl. Acad. Sci. USA* **115**, E822–E831 (2018).
23. D'Ario, M. et al. Cell size controlled in plants using DNA content as an internal scale. *Science* **372**, 1176–1181 (2021).

24. Refahi, Y. et al. A multiscale analysis of early flower development in Arabidopsis provides an integrated view of molecular regulation and growth control. *Dev. Cell* **56**, 540–556.e8 (2021).
25. Kwiatkowska, D. & Dumais, J. Growth and morphogenesis at the vegetative shoot apex of Anagallis arvensis L. *J. Exp. Bot.* **54**, 1585–1595 (2003).
26. Barbier de Reuille, P. et al. MorphoGraphX: A platform for quantifying morphogenesis in 4D. *Elife* **4**, 05864 (2015).
27. Smyth, D. R., Bowman, J. L. & Meyerowitz, E. M. Early flower development in Arabidopsis. *Plant Cell* **2**, 755–767 (1990).
28. Breuil-Broyer, S. et al. High-resolution boundary analysis during Arabidopsis thaliana flower development. *Plant J.* **38**, 182–192 (2004).
29. Cheddadi, I., Génard, M., Bertin, N. & Godin, C. Coupling water fluxes with cell wall mechanics in a multicellular model of plant development. *PLoS Comput. Biol.* **15**, e1007121 (2019).
30. Ortega, J. K. E. Augmented Growth Equation for Cell Wall Expansion. *Plant Physiol.* **79**, 318–320 (1985).
31. Gisel, A., Barella, S., Hempel, F. D. & Zambryski, P. C. Temporal and spatial regulation of symplastic trafficking during development in Arabidopsis thaliana apices. *Development* **126**, 1879–1889 (1999).
32. Léon-Kloosterziel, K. M. et al. Isolation and characterization of abscisic acid-deficient *Arabidopsis* mutants at two new loci. *Plant J.* **10**, 655–661 (1996).
33. Hamant, O., Das, P. & Burian, A. Time-lapse imaging of developing shoot meristems using a confocal laser scanning microscope. in *Plant Cell Morphogenesis* (eds. Cvrčková, F. & Žárský, V.) vol. **1992** 257–268 (Springer New York, New York, NY, 2019).
34. Tian, C. et al. A gene expression map of shoot domains reveals regulatory mechanisms. *Nat. Commun.* **10**, 141 (2019).
35. Goswami, R. et al. Mechanical shielding in plant nuclei. *Curr. Biol.* **30**, 2013–2025 (2020).
36. Ascenzi, R. & Gantt, J. S. Molecular genetic analysis of the drought-inducible linker histone variant in Arabidopsis thaliana. *Plant Mol. Biol.* **41**, 159–169 (1999).
37. Rutowicz, K. et al. A specialized histone H1 variant is required for adaptive responses to complex abiotic stress and related DNA methylation in arabidopsis. *Plant Physiol.* **169**, 2080–2101 (2015).
38. Tarancón, C., González-Grandío, E., Oliveros, J. C., Nicolas, M. & Cubas, P. A conserved carbon starvation response underlies bud dormancy in woody and herbaceous species. *Front. Plant Sci.* **8**, 788 (2017).
39. Cadman, C. S. C., Toorop, P. E., Hilhorst, H. W. M. & Finch-Savage, W. E. Gene expression profiles of Arabidopsis Cvi seeds during dormancy cycling indicate a common underlying dormancy control mechanism. *Plant J.* **46**, 805–822 (2006).
40. Rutowicz, K. et al. Linker histones are fine-scale chromatin architects modulating developmental decisions in Arabidopsis. *Genome Biol.* **20**, 157 (2019).
41. Molz, F. J. & Boyer, J. S. Growth-induced water potentials in plant cells and tissues. *Plant Physiol.* **62**, 423–429 (1978).
42. Nonami, H. & Boyer, J. S. Direct demonstration of a growth-induced water potential gradient. *Plant Physiol.* **102**, 13–19 (1993).
43. Tian, C. et al. An organ boundary-enriched gene regulatory network uncovers regulatory hierarchies underlying axillary meristem initiation. *Mol. Syst. Biol.* **10**, 755–755 (2014).
44. Aida, M. & Tasaka, M. Genetic control of shoot organ boundaries. *Curr. Opin. Plant Biol.* **9**, 72–77 (2006).
45. Wang, Y. Stem cell basis for fractal patterns: axillary meristem initiation. *Front. Plant Sci.* **12**, 805434 (2021).
46. Peaucelle, A. et al. Pectin-induced changes in cell wall mechanics underlie organ initiation in Arabidopsis. *Curr. Biol.* **21**, 1720–1726 (2011).
47. Cui, F. et al. Dissecting abscisic acid signaling pathways involved in cuticle formation. *Mol. Plant* **9**, 926–938 (2016).
48. Ramachandran, P. et al. Abscisic acid signaling activates distinct VND transcription factors to promote xylem differentiation in Arabidopsis. *Curr. Biol.* **31**, 3153–3161.e5 (2021).
49. Grondin, A. et al. Aquaporins contribute to ABA-triggered stomatal closure through OST1-mediated phosphorylation. *Plant Cell* **27**, 1945–1954 (2015).
50. Mao, Z. & Sun, W. *Arabidopsis* seed-specific vacuolar aquaporins are involved in maintaining seed longevity under the control of *ABSCISIC ACID INSENSITIVE 3*. *J. Exp. Bot.* **66**, 4781–4794 (2015).
51. Hachez, C. et al. The *arabidopsis* abiotic stress-induced TSPO-related protein reduces cell-surface expression of the aquaporin PIP2;7 through protein-protein interactions and autophagic degradation. *Plant Cell* **26**, 4974–4990 (2014).
52. Long, Y. et al. Cellular heterogeneity in pressure and growth emerges from tissue topology and geometry. *Curr. Biol.* **30**, 1504–1516 (2020).
53. Asnacios, A. & Hamant, O. The mechanics behind cell polarity. *Trends Cell Biol.* **22**, 584–591 (2012).
54. Shapiro, B. E., Tobin, C., Mjolsness, E. & Meyerowitz, E. M. Analysis of cell division patterns in the Arabidopsis shoot apical meristem. *Proc. Natl. Acad. Sci. USA* **112**, 4815–4820 (2015).
55. Alt, S., Ganguly, P. & Salbreux, G. Vertex models: from cell mechanics to tissue morphogenesis. *Philos. Trans. R. Soc. B* **372**, 20150520 (2017).
56. Lockhart, J. A. An analysis of irreversible plant cell elongation. *J. Theor. Biol.* **8**, 264–275 (1965).
57. Forterre, Y. Chapter 1. Basic soft matter for plants. in *Soft Matter Series* (eds. Jensen, K. & Forterre, Y.) 1–65 (Royal Society of Chemistry, Cambridge, 2022).
58. Kiss, A. et al. Segmentation of 3D images of plant tissues at multiple scales using the level set method. *Plant Methods* **13**, 114 (2017).
59. Fernandez, R. et al. Imaging plant growth in 4D: robust tissue reconstruction and lineaging at cell resolution. *Nat. Methods* **7**, 547–553 (2010).
60. Ourselin, S., Roche, A., Prima, S. & Ayache, N. Block matching: A general framework to improve robustness of rigid registration of medical images. in *Medical Image Computing and Computer-Assisted Intervention – MICCAI 2000* (eds. Delp, S. L., DiGoia, A. M. & Jaramaz, B.) vol. **1935**, 557–566 (Springer Berlin Heidelberg, Berlin, Heidelberg, 2000).
61. Schroeder, W. J. et al. *The Visualization Toolkit: An Object-Oriented Approach to 3D Graphics; [Visualize Data in 3D - Medical, Engineering or Scientific; Build Your Own Applications with C++, Tcl, Java or Python; Includes Source Code for VTK (Supports UNIX, Windows and Mac)]*. (Kitware, Inc, Clifton Park, NY, 2006).
62. Theisel, H., Rossl, C., Zayer, R. & Seidel, H.-P. Normal based estimation of the curvature tensor for triangular meshes. in *12th Pacific Conference on Computer Graphics and Applications, 2004. PG 2004. Proceedings*. 288–297 (IEEE, Seoul, Korea, 2004).

Acknowledgements

We thank the Mosaic and MechanoDevo teams at the RDP lab for insightful discussion, and Platim for help with imaging. We thank Johanna Dickmann for helpful comments on this manuscript. We thank Àngela Carrió-Seguí for sharing the *aba2-1* mutant. This work was supported by an EMBO Long Term Fellowship (#ALTF1-2020 to J.A-S.) and by the European Research Council (ERC-2021-AdG-101019515 "Musix" to O.H.). I.C. and C.G. were supported by the ANR project "Hydrofield".

Author contributions

Conceptualization: J.A.S., I.C., C.G., and O.H. Methodology: J.A.S., I.C., A.K., G.C., M.L., S.D., and C.L. Funding acquisition: J.A.S., G.C., and O.H. Project administration: C.G. and O.H. Supervision: C.G. and O.H. Writing – original draft: J.A.S., I.C., and O.H. Writing – review & editing: J.A.S., I.C., A.K., G.C., C.G., and O.H.

Competing interests
The authors declare no competing interests.

Additional information
Supplementary information The online version contains supplementary material available at https://doi.org/10.1038/s41467-024-51099-x.

Correspondence and requests for materials should be addressed to Juan Alonso-Serra or Olivier Hamant.

Peer review information *Nature Communications* thanks Robert Sablowski, Malcolm Bennett and the other anonymous, reviewer(s) for their contribution to the peer review of this work. A peer review file is available.